

Particle Morphology and Lithium Segregation to Surfaces of the $\text{Li}_7\text{La}_3\text{Zr}_2\text{O}_{12}$ Solid Electrolyte

Pieremanuele Canepa,^{*,†} James A. Dawson,[†] Gopalakrishnan Sai Gautam,[‡] Joel M. Statham,[†] Stephen C. Parker,[†] and M. Saiful Islam^{*,†}

[†]*Department of Chemistry, University of Bath, Bath, BA2 7AY, UK*

[‡]*Department of Mechanical and Aerospace Engineering, Princeton University, Princeton, NJ 08544, USA*

E-mail: p.canepa@bath.ac.uk; m.s.islam@bath.ac.uk

Abstract

Solid electrolytes for solid-state Li-ion batteries are stimulating considerable interest for next-generation energy storage applications. The $\text{Li}_7\text{La}_3\text{Zr}_2\text{O}_{12}$ garnet-type solid electrolyte has received appreciable attention as a result of its high ionic conductivity. However, several challenges for the successful application of solid-state devices based on $\text{Li}_7\text{La}_3\text{Zr}_2\text{O}_{12}$ remain, such as dendrite formation and maintaining physical contact at interfaces over many Li intercalation/extraction cycles. Here, we apply first-principles density functional theory to provide insights into the $\text{Li}_7\text{La}_3\text{Zr}_2\text{O}_{12}$ particle morphology under various physical and chemical conditions. Our findings indicate Li segregation at the surfaces, suggesting Li-rich grain boundaries at typical synthesis and sintering conditions. On the basis of our results, we propose practical strategies to curb Li segregation at the $\text{Li}_7\text{La}_3\text{Zr}_2\text{O}_{12}$ interfaces. This approach can be extended to other Li-ion conductors for the design of practical energy storage devices.

Introduction

The commercial Li-ion battery, which relies on liquid electrolytes, is now the workhorse behind the mobile electronics industry.^{1–5} Unfortunately, a practical limit of what can be achieved with the current Li-ion technology is encountered when the focus shifts to electric vehicles.^{2,4–6} One promising avenue to improve the energy and power densities of Li-ion batteries, while enhancing their safety, consists of replacing the flammable liquid electrolyte with a solid electrolyte capable of efficiently shuttling Li ions between electrodes.^{7–21}

To facilitate this transition, the Li-ion conductivity of solid electrolytes must be competitive to that of their liquid analogs.^{12,16} While significant attention is still devoted to intrinsic Li⁺ conductivity in solid electrolytes, many challenges remain for future solid-state applications.^{5,22–30} The most pressing challenges are finding solid electrolytes that are electrochemically stable against electrodes, maintaining physical contact between components over many Li intercalation/extraction cycles and suppressing Li-dendrite formation.

The Li₇La₃Zr₂O₁₂ garnet-type electrolyte has received significant attention due to its high ionic conductivity (10^{-6} – 10^{-3} S cm⁻¹) achieved by a variety of doping strategies,^{7,8,10,11,31–36} but most importantly because of its perceived stability against the Li-metal anode.^{25,27,29,37–41}

However, the failure of polycrystalline Li₇La₃Zr₂O₁₂ in solid-state battery prototypes comprised of Li-metal anodes has been the subject of several studies.^{25,28,38,40–43} It has been observed²⁹ that once Li fills a crack in Li₆La₃ZrTaO₁₂, fresh electro-deposited Li is extruded to the available surface. Tests with Li-metal/Li₇La₃Zr₂O₁₂/Li-metal cells showed that only small current densities of ~ 0.5 mA cm⁻² could be tolerated before dendrite failure.^{27,44} Rationalising the mechanisms behind the propagation of dendrites in Li₇La₃Zr₂O₁₂ is a major challenge.

In parallel, sintering strategies to maximise the bulk transport in ceramic materials are routinely applied. While high temperature densification enhances ion transport, the extent of morphological transformations of the electrolyte particles is still unclear. Kerman *et al.*²⁷ highlighted the connection between the processing conditions of Li₇La₃Zr₂O₁₂ and its particle

morphology and size. Kingon *et al.*⁴⁵ demonstrated that ceramics containing volatile cations, such as $\text{Li}_7\text{La}_3\text{Zr}_2\text{O}_{12}$, become Li deficient upon sintering.

These experimental observations indicate that it is crucial to understand the variation of the $\text{Li}_7\text{La}_3\text{Zr}_2\text{O}_{12}$ morphology as a function of chemical and physical properties (composition and temperature).

In this study, we develop a phenomenological model based on first-principles calculations to determine the composition of $\text{Li}_7\text{La}_3\text{Zr}_2\text{O}_{12}$ particles, while the chemical environment of Li, La, Zr and O, voltage and/or the temperature are varied. Rationalising the particle morphology of solid electrolytes contributes towards a deeper understanding of several critical phenomena, including the Li^+ conductivity at grain boundaries and the propagation of dendrites during battery operation. Indeed, our results predict significant Li accumulation at the exterior of the $\text{Li}_7\text{La}_3\text{Zr}_2\text{O}_{12}$ particles when we mimic reducing high-temperature synthesis conditions.

Based on our computational insights, we propose practical strategies to engineer the chemical compositions of the particles, providing a greater control of the complex chemistry of $\text{Li}_7\text{La}_3\text{Zr}_2\text{O}_{12}$. These general design strategies can be extended to other solid electrolytes and electrode materials.

Results

Phase stability and chemical domains

We first consider the relative stability of the $\text{Li}_7\text{La}_3\text{Zr}_2\text{O}_{12}$ tetragonal (space group $I4_1/acd$) and high-temperature cubic ($Ia3\bar{d}$) polymorphs. The computed lattice constants ($a = 13.204$ and $c = 12.704$ Å) of the tetragonal phase compare well with the experimental data ($a = 13.134$ and $c = 12.663$ Å).⁴⁶ Figure 1a shows the decomposition of $\text{Li}_7\text{La}_3\text{Zr}_2\text{O}_{12}$ into $\text{Li}_6\text{Zr}_2\text{O}_7 + \text{La}_2\text{O}_3 + \text{Li}_8\text{ZrO}_6$, revealing the metastability of both the cubic (~ 22 meV/atom above the stability line at 0 K) and tetragonal (~ 7 meV/atom) polymorphs, in agreement with

previous density functional theory (DFT) predictions.^{47,48}

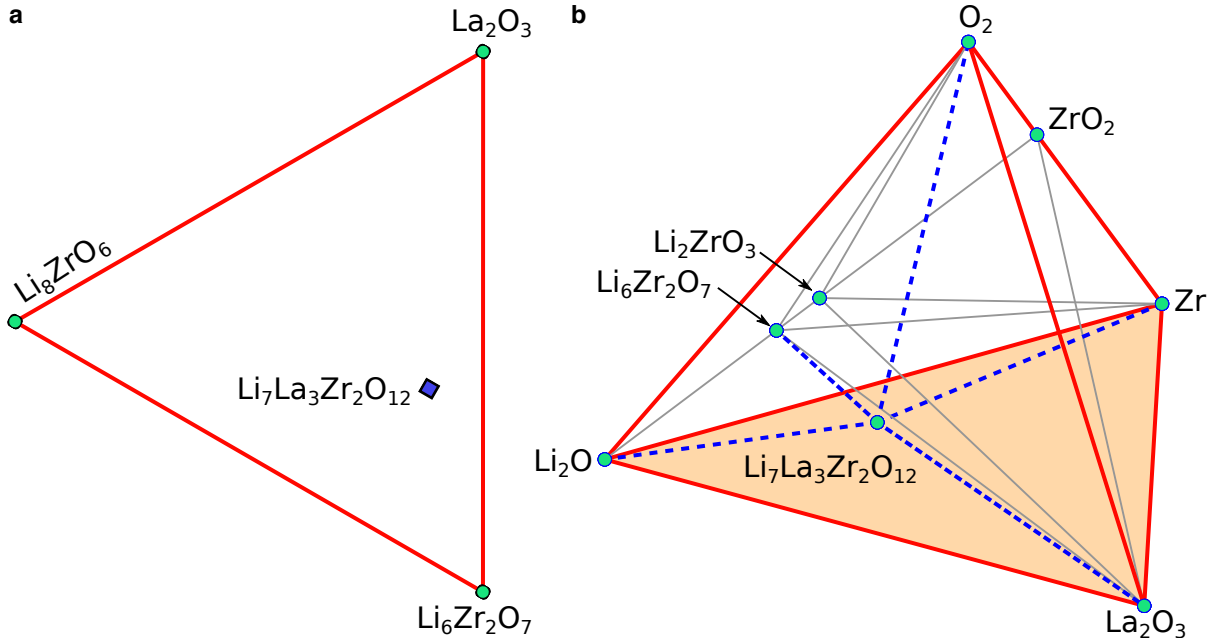


Figure 1: (a) La_2O_3 – $\text{Li}_6\text{Zr}_2\text{O}_7$ – Li_8ZrO_6 projection of the quaternary Li–La–O–Zr phase diagram showing the decomposition products of the metastable $\text{Li}_7\text{La}_3\text{Zr}_2\text{O}_{12}$ (blue diamond), which are $\text{Li}_6\text{Zr}_2\text{O}_7$, La_2O_3 and Li_8ZrO_6 . (b) Compound Li_2O – La_2O_3 – Zr – O_2 phase diagrams where $\text{Li}_7\text{La}_3\text{Zr}_2\text{O}_{12}$ is assumed to be stable. Green dots display the stable phases, while red, blue and grey lines identify equilibrium tie lines. Dash blue lines mark tie lines shared by $\text{Li}_7\text{La}_3\text{Zr}_2\text{O}_{12}$ and some of the binary precursors used in its synthesis. Both phase diagrams are computed from DFT data at 0 K and combined with existing entries in the Materials Project database.⁴⁹

The degree of metastability of the tetragonal phase is small enough that the compound can be stabilised by thermal effects, which explains the success of high-temperature (> 600 °C) phase-pure synthesis.^{8,11} It is assumed that the chemical decomposition of $\text{Li}_7\text{La}_3\text{Zr}_2\text{O}_{12}$ into $\text{Li}_6\text{Zr}_2\text{O}_7 + \text{La}_2\text{O}_3 + \text{Li}_8\text{ZrO}_6$ requires a major coordination rearrangement of Zr and La, thereby kinetically preventing $\text{Li}_7\text{La}_3\text{Zr}_2\text{O}_{12}$ from decomposing. Therefore, we assume that $\text{Li}_7\text{La}_3\text{Zr}_2\text{O}_{12}$ is thermodynamically stable (see phase diagram in Figure 1b).

Identifying the phases in equilibrium with $\text{Li}_7\text{La}_3\text{Zr}_2\text{O}_{12}$ (Figure 1b) allows us to set the bounds of chemical potentials of each element, thus providing a thermodynamic framework to calculate meaningful non-stoichiometric surface energies (see Method section). Figure 1b illustrates the phases in equilibrium with $\text{Li}_7\text{La}_3\text{Zr}_2\text{O}_{12}$, which show that only La_2O_3 ,

$\text{Li}_6\text{Zr}_2\text{O}_7$, Li_2O , O_2 and Zr are in direct equilibrium with the solid electrolyte. Experimentally, the binary compounds La_2O_3 , Li_2CO_3 (LiOH or Li_2O)²⁹ and ZrO_2 are used as precursors for the synthesis of $\text{Li}_7\text{La}_3\text{Zr}_2\text{O}_{12}$.^{8,29} In addition, when $\text{Li}_7\text{La}_3\text{Zr}_2\text{O}_{12}$ is assumed to be stable, Li_8ZrO_6 becomes metastable in the Li-La-Zr-O phase diagram (Figure 1b).

Our discussion moves to the definition of the relevant chemical potentials, which have to be rigorously defined to accurately calculate the energies of non-stoichiometric surface structures (see Eq. 1). From thermodynamic arguments, any combination of three compounds in equilibrium with $\text{Li}_7\text{La}_3\text{Zr}_2\text{O}_{12}$ define distinct chemical potentials (μ) for the elements O, La, Li and Zr. In this study, we consider two different chemical regimes, i.e. *oxidising* and *reducing*. The tetrahedron composed of $\text{Li}_7\text{La}_3\text{Zr}_2\text{O}_{12}$, La_2O_3 , Li_2O and O_2 mimics the *oxidising* and experimental synthesis conditions of $\text{Li}_7\text{La}_3\text{Zr}_2\text{O}_{12}$. In contrast, we consider a *reducing* environment as defined by $\text{Li}_7\text{La}_3\text{Zr}_2\text{O}_{12}$ being in equilibrium with Zr metal, La_2O_3 and Li_2O , which corresponds to experimental sintering conditions. A detailed derivation and the bounds of the chemical potential used for each species are summarised in Section 1 and Table S1 of the Supplementary Information (SI).

Although Zr forms oxides with multiple oxidation states, such as ZrO and Zr_2O as reported by Chen *et al.*,⁵⁰ Zr is not redox active in $\text{Li}_7\text{La}_3\text{Zr}_2\text{O}_{12}$. Therefore, Zr-metal and ZrO_2 represent valid reference states for the μ_{Zr} in reducing (Zr^0) and oxidising (Zr^{4+}) environments, respectively.

Surface structures and energies

Surfaces of solid electrolytes are important to their electrochemical properties, particularly due to the presence of active interfaces within intercalation batteries. The $\text{Li}_7\text{La}_3\text{Zr}_2\text{O}_{12}$ cubic polymorph provides the highest ionic conductivity.^{11,47,51} However, accounting for the Li disorder presents a major computational complexity when creating representative surface structures. Thus, we consider the tetragonal polymorph, which constitutes a distinct ordering of Li sites, as the reference structure for creating our surface models.

Figure 2 depicts the atomic arrangement of the Li-terminated (010) surface of $\text{Li}_7\text{La}_3\text{Zr}_2\text{O}_{12}$, highlighting the significant reconstruction of the Li and O layers, respectively. The dotted

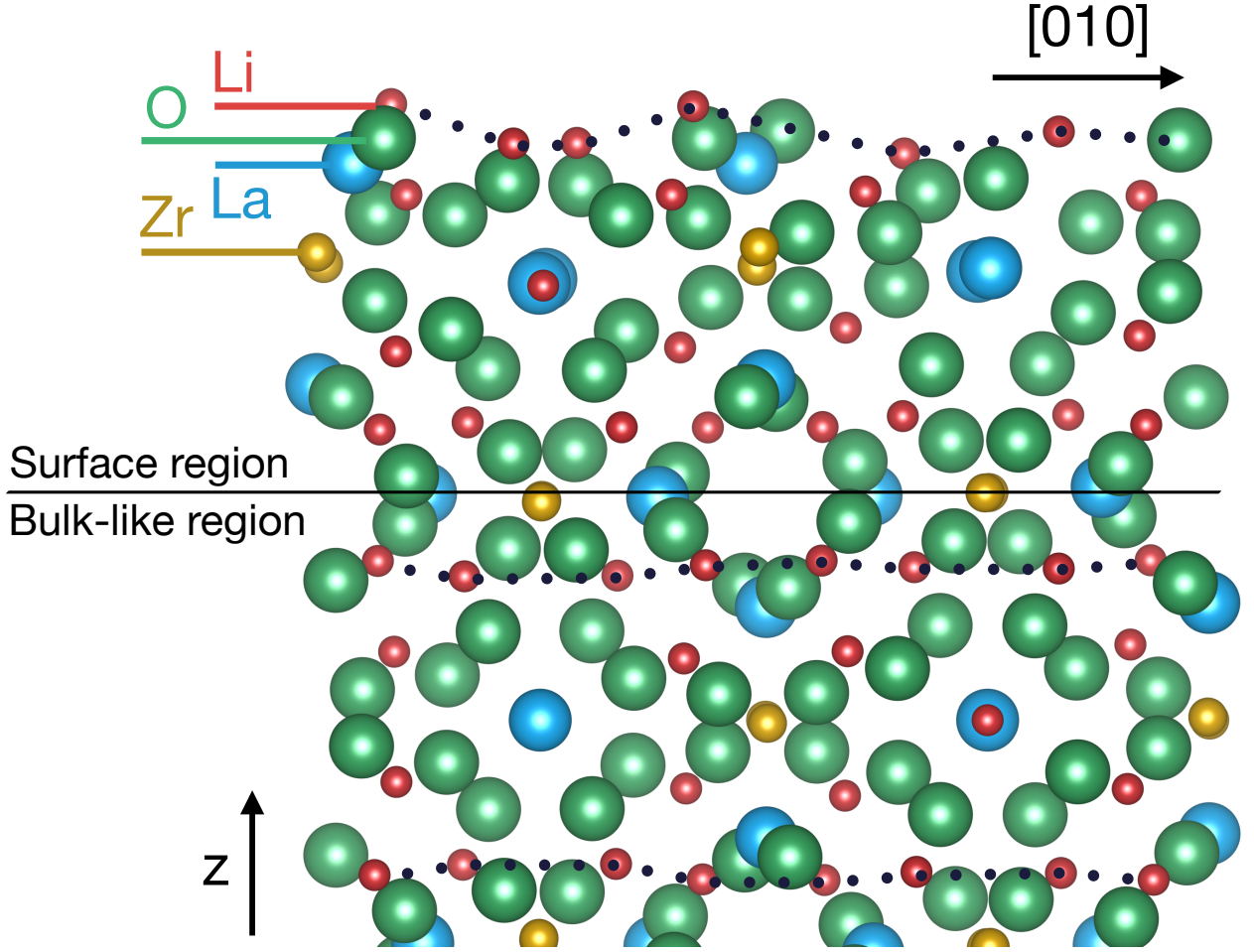


Figure 2: Sideview of the non-stoichiometric (010) Li-terminated surface of $\text{Li}_7\text{La}_3\text{Zr}_2\text{O}_{12}$. Li atoms are in red, O in green, La in blue and Zr in gold. Solid lines identify the arrangement of each atom plane along the non-periodic z axis. The black line marks the separation between the bulk-like region from the surface region. The black dotted lines are guides for the eye to highlight the change in the local Li symmetry upon surface reconstruction.

lines in Figure 2 are a guide for the eye to illustrate the loss of symmetry of the Li environment at the surface compared to the bulk region. Figure 2 shows that La layers overlap with “rumpled” oxygen layers, which contribute to stabilise La-terminated surfaces, as discussed in the following paragraphs. In the case of Zr ions, the oxygen coordination environment in the surface slab show insignificant deviation from the octahedral coordination within bulk $\text{Li}_7\text{La}_3\text{Zr}_2\text{O}_{12}$, in qualitative agreement with the lack of surface reconstruction observed in

ZrO₂.⁵²

It is known that for a given Miller index several surface terminations may be possible since the bulk can be cleaved at different planes, as shown in Figure 2. The relative stability of each surface model is defined by their surface energy (γ , Eq. 1). Figure 3 depicts the computed γ values of a number of stoichiometric and non-stoichiometric La, Li, O and Zr-terminated surfaces of Li₇La₃Zr₂O₁₂. Non-stoichiometric surfaces refer to surfaces where the stoichiometry deviates in composition from the bulk. The surface energies of symmetry-related Miller index surfaces (e.g., (100) \approx (010) \approx (001)) are detailed in Table S2. As introduced in Section , the chemical potentials, μ_i , for calculating γ of non-stoichiometric surfaces are set to reducing conditions (i.e., $\mu_{\text{La}} \approx \mu_{\text{La}}$ in La₂O₃, $\mu_{\text{Li}} \approx \mu_{\text{Li}}$ in Li₂O, and $\mu_{\text{Zr}} \approx \mu_{\text{Zr}}$ in Zr metal), see Figure 1b and Section 1 of the SI.

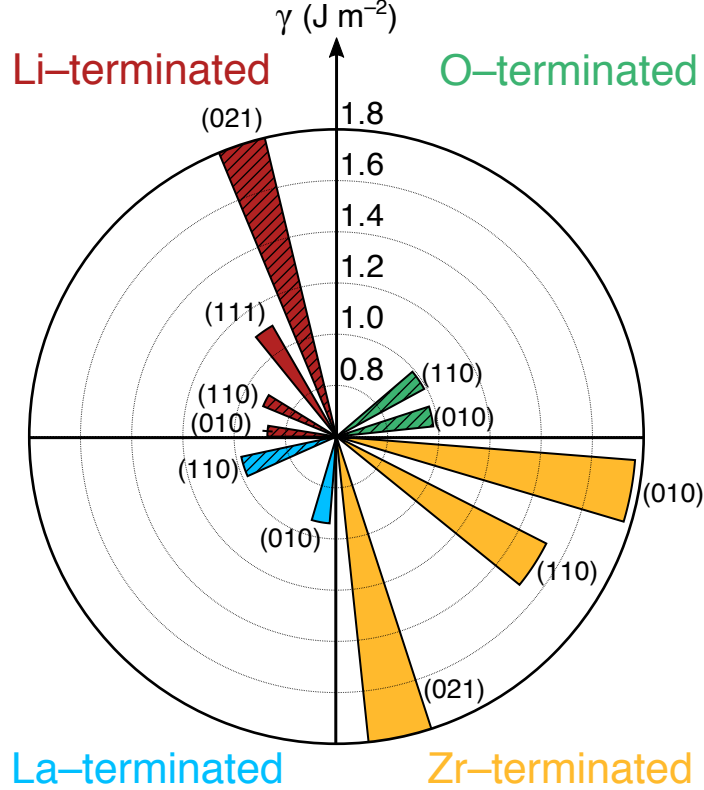


Figure 3: Surface energies γ (J m⁻²) of La (blue), Li (red), O (green) and Zr (yellow) -terminated surfaces of Li₇La₃Zr₂O₁₂. Hatched bars indicate non-stoichiometric surfaces, whose surface energies are derived using the chemical potentials from Figure 1b. The chemical potentials of Li, La and Zr are fixed by Li₂O, La₂O₃ and Zr metal, respectively, corresponding to reducing conditions (details in Section).

Figure 3 shows three main features: i) Zr-terminated surfaces show the highest surface energy γ ($> 1.5 \text{ J m}^{-2}$), ii) certain Li-terminated surfaces possess significantly lower γ ($\sim 0.87 \pm 0.02 \text{ J m}^{-2}$ for the (010) surface), in good agreement with previous work.⁴⁸ iii) La- and O-terminated surfaces show similar surface energies, as indicated by γ 0.98 J m^{-2} and 0.99 J m^{-2} for the La- and O-terminated (110) surfaces, respectively.

Although the surface structures are obtained from the tetragonal phase, we find identical surface energies for symmetry inequivalent surfaces (see Table S1 and Figure S1). For example, the surface energy ($\sim 1.77 \text{ J m}^{-2}$) of the Zr-terminated (010) surface is identical to the (001) and (100) surfaces, which is typically not found for tetragonal structures. This suggests the similarity between the tetragonal and cubic phases of $\text{Li}_7\text{La}_3\text{Zr}_2\text{O}_{12}$ and indicates that the Li ordering, which affects the relative stability of the bulk tetragonal and cubic phases, has only a negligible impact on the relative symmetry and energetics of $\text{Li}_7\text{La}_3\text{Zr}_2\text{O}_{12}$ surfaces. Notably, the c/a ratio exhibited by the tetragonal phase (~ 0.96 from experimental lattice constants, see Section) signifies the “small” tetragonal distortion in $\text{Li}_7\text{La}_3\text{Zr}_2\text{O}_{12}$.

Effects of oxygen environment and temperature on surfaces

With the aim of understanding the interplay between compositional and temperature effects on the morphology of $\text{Li}_7\text{La}_3\text{Zr}_2\text{O}_{12}$, we now move our attention to trends of surface energy as a function of temperature and oxygen composition. To include temperature dependence in our model, we apply a thermodynamic framework (detailed in the Method section) that connects changes in the O_2 chemical potential, μ_{O_2} , directly to temperature.⁵³ This approximation is valid as the $\text{Li}_7\text{La}_3\text{Zr}_2\text{O}_{12}$ electrolyte is in contact with an oxygen environment during its synthesis and sintering.

With $\mu_{\text{O}} = \frac{1}{2}\mu_{\text{O}_2}$, μ_{O} sets the surface energy of non-stoichiometric surfaces, as indicated in Eq. 2. Note that under both oxidising and reducing conditions (Section), the chemical potentials of La and Li are set by La_2O_3 and Li_2O , respectively. All the non-stoichiometric surfaces studied here are either oxygen rich or poor (see Method section). High μ_{O} (or μ_{O_2})

represents low-temperature situations and a highly oxidative environment, where oxygen molecules “condense” on the surfaces of $\text{Li}_7\text{La}_3\text{Zr}_2\text{O}_{12}$. In contrast, higher temperatures (i.e., more negative μ_{O}) signify reducing conditions, where oxygen atoms become volatile and leave the surface as O_2 gas, which is equivalent to $\text{Li}_7\text{La}_3\text{Zr}_2\text{O}_{12}$ being in equilibrium with Zr metal.

Figure 4 shows the variation of the surface energy for a number of non-stoichiometric surfaces as a function of temperature, or its equivalent μ_{O} , corresponding to an oxygen partial pressure of 1 atm.

A number of important observations can be drawn from Figure 4. i) The Li-terminated (010) surface has the lowest γ (as in Figure 3) and the La-terminated (010) stoichiometric surface has the highest γ for temperatures higher than 25 °C. The negative slope of each line signifies that all the surfaces are oxygen deficient. While studying non-stoichiometric surfaces, we have focused on La, Li and O deficient scenarios, as they are most likely to develop at high temperatures.^{54,55} In order to maintain the electroneutrality of oxygen-terminated surfaces, oxygen vacancies were introduced to compensate the removal of cations (details are provided in the Method section). ii) The stability of the Li-terminated (010) surfaces in comparison to other terminations is significant. iii) At temperatures higher than 300 °C, the O-terminated (010) and (110) surfaces become more stable than the (110) Li-terminated surface. This result is also found for the (100), (001), (011) and (101) Li-terminated facets. iv) Above 750 °C, the negative γ of (010) Li-terminated surface (as seen in Figure 4) is indicative of the instability of bulk $\text{Li}_7\text{La}_3\text{Zr}_2\text{O}_{12}$, and may be linked to the melting of $\text{Li}_7\text{La}_3\text{Zr}_2\text{O}_{12}$ particles.

Environment dependent particle morphologies

By combining our surface energies of various surface facets at distinct chemical compositions (Figures 3 and 4), we can implement the Wulff construction to derive the $\text{Li}_7\text{La}_3\text{Zr}_2\text{O}_{12}$ equilibrium particle morphology at synthesis conditions.

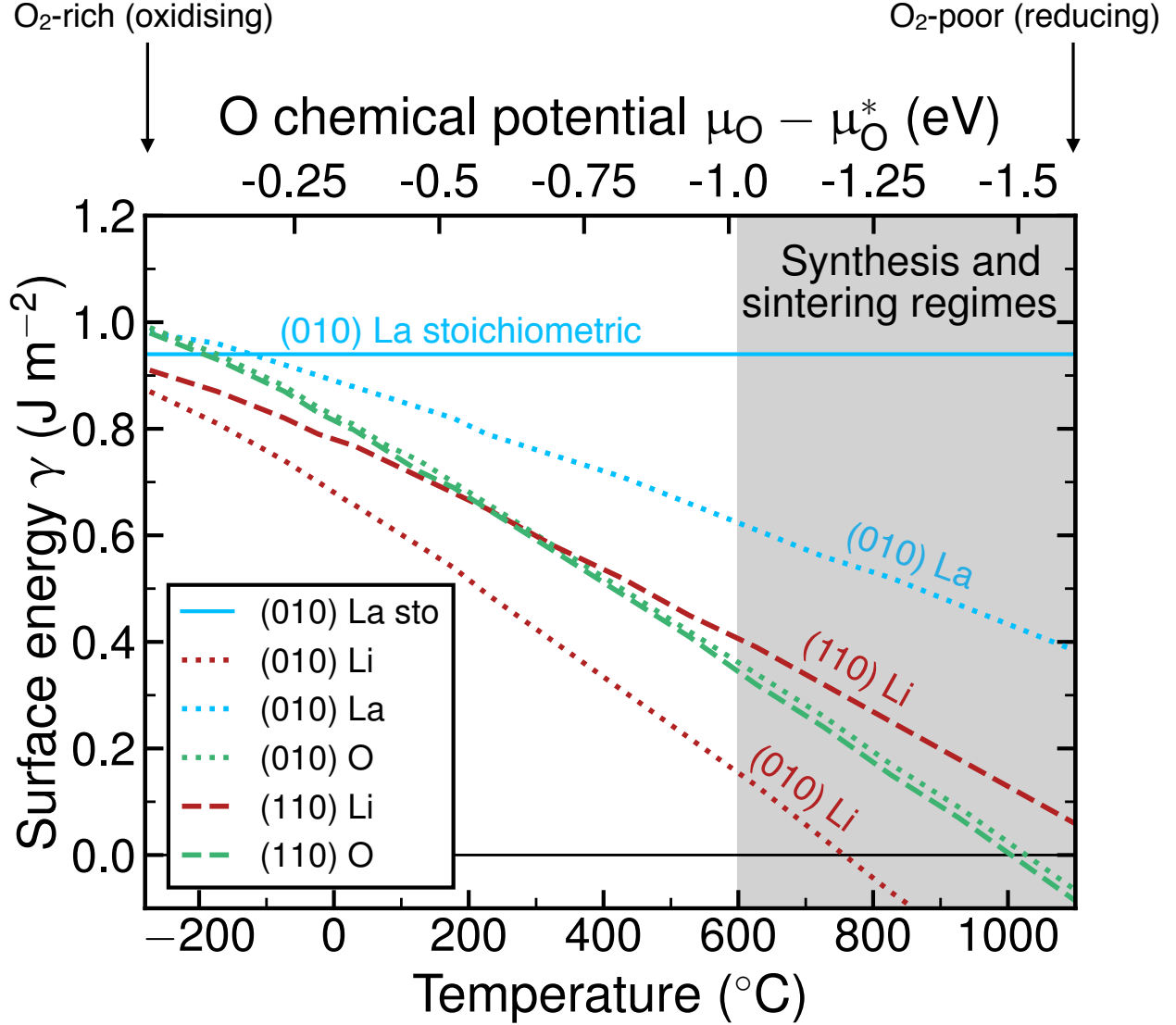


Figure 4: Surface energy γ of La (blue), Li (red) and O (green) -terminated $\text{Li}_7\text{La}_3\text{Zr}_2\text{O}_{12}$ surfaces vs temperature and oxygen chemical potential μ_O . The blue horizontal line indicates the stoichiometric La-terminated surface energy. The zero (eV) in the μ_O scale is normalised against the reference state μ_O^* and is detailed in the SI. μ_O near 0 eV relates to oxygen-rich (or oxidising) regimes, whereas more negative oxygen chemical potentials are oxygen-poor (or reducing) conditions. The grey shading marks the experimental temperature window for synthesis and sintering of $\text{Li}_7\text{La}_3\text{Zr}_2\text{O}_{12}$.¹¹ The chemical potentials of Li and La are fixed by Li_2O and La_2O_3 , respectively, while μ_O is allowed to vary.

Figure 5 depicts the change of the particle equilibrium morphology as a function of temperature.

At room temperature (~ 24 °C), the equilibrium $\text{Li}_7\text{La}_3\text{Zr}_2\text{O}_{12}$ particle morphology is dominated by the (001), (101) and (110) surfaces. For temperatures greater than 600 °C

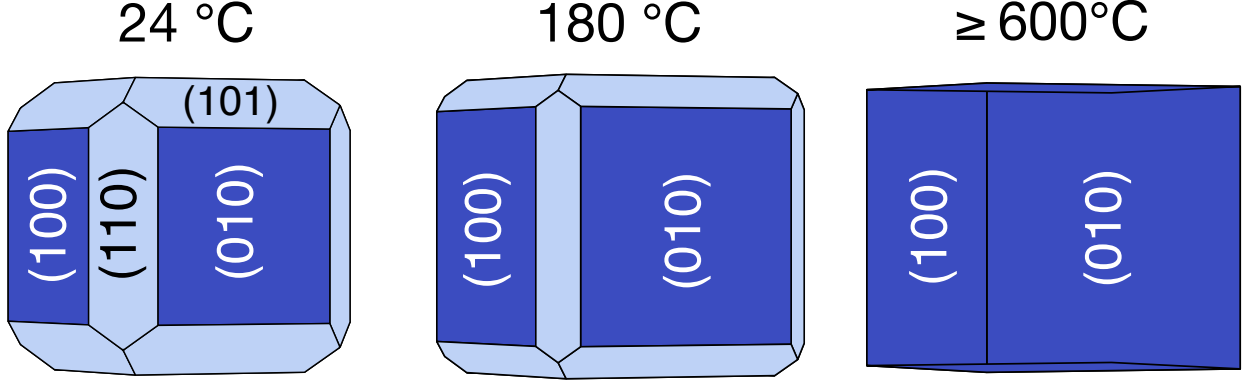


Figure 5: Variation in the $\text{Li}_7\text{La}_3\text{Zr}_2\text{O}_{12}$ equilibrium morphology with increasing temperature. The particles are expected to be Li-terminated, as suggested in Figure 4. Labels identify the surface planes of interest.

(and $< 750\text{ }^\circ\text{C}$), $\text{Li}_7\text{La}_3\text{Zr}_2\text{O}_{12}$ particles should assume a cubic shape dominated by the (100) and (010) surfaces, as seen in Figure 5.

At $24\text{ }^\circ\text{C}$ and intermediate temperatures ($\sim 180\text{ }^\circ\text{C}$), the (110) Li-terminated surface contributes to the overall particle shape. However, an increase in oxygen composition on the surface of the $\text{Li}_7\text{La}_3\text{Zr}_2\text{O}_{12}$ particles will be also observed, as shown by the increased stability of the (110) oxygen-terminated surfaces over (110) Li-terminations, as seen in Figure 4 at temperatures above $300\text{ }^\circ\text{C}$.

Tuning the synthesis conditions of $\text{Li}_7\text{La}_3\text{Zr}_2\text{O}_{12}$

We now discuss the surface phase diagram obtained by varying the chemical composition of $\text{Li}_7\text{La}_3\text{Zr}_2\text{O}_{12}$. This analysis contributes to understanding the experimental synthesis conditions to achieve the desired chemical composition of the particle surfaces.

Computing a complete surface phase diagram represents a formidable exercise given the large compositional space for the non-stoichiometric terminations accompanied by the large number of atomic arrangements of partially occupied terminating layers. Thus, we limit the discussion of the surface phase diagram to the $\text{Li}_7\text{La}_3\text{Zr}_2\text{O}_{12}$ surfaces in Figure 3. Li-rich and Li-poor conditions correspond to Li_2O (reducing conditions) and $\text{Li}_6\text{Zr}_2\text{O}_7$ (oxidising conditions), respectively, while Zr-rich is equivalent to Zr metal (reducing) and Zr-poor to

O₂ gas (oxidising).

Figure 6 shows the surface phase diagram at 0 K by varying the Li (μ_{Li}) and Zr (μ_{Zr}) composition. We find that regions of low μ_{Li} and μ_{Zr} are consistently dominated by the

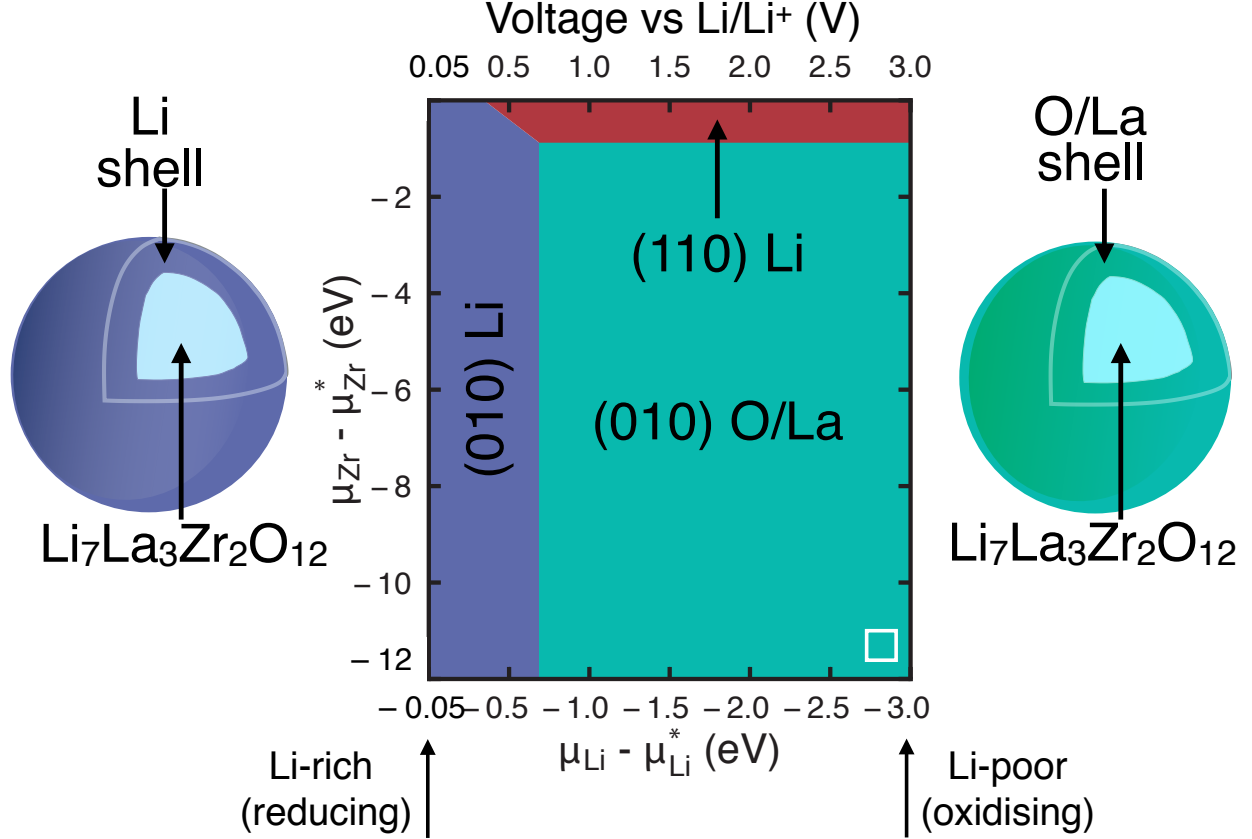


Figure 6: Surface phase diagram at 0 K of $\text{Li}_7\text{La}_3\text{Zr}_2\text{O}_{12}$ and schematic representations of particle morphologies at different chemical conditions. Stable surfaces and chemical terminations as a function of μ_{Li} and μ_{Zr} . The white square identifies the compositional Li–Zr conditions where $\text{Li}_7\text{La}_3\text{Zr}_2\text{O}_{12}$ is commonly synthesised. Zr-rich is equivalent to Zr metal (Zr-poor is O₂ gas), whereas Li-rich is Li metal (and Li-poor is $\text{Li}_6\text{Zr}_2\text{O}_7$). The voltage evolution vs Li/Li* (with $V = -\mu_{\text{Li}} \cdot e^-$) is also shown. The chemical potential scales are referenced against the reference states μ_{Li}^* (Li_2O) and μ_{Zr}^* (Zr metal).

(010) O- and La-terminated surfaces. At more positive μ_{Li} and μ_{Zr} (near Li-rich and Zr-rich conditions), the (010) Li-terminated surfaces are stable. In fact, the (010) O- and La-terminated surfaces have similar surface energies ~ 0.94 and $\sim 0.98 \text{ J m}^{-2}$, respectively (see Figure 3), as the La ions exposed are surrounded by a O sub-layer. The La/O or Li segregations at the surface of the particles of $\text{Li}_7\text{La}_3\text{Zr}_2\text{O}_{12}$ (at specific μ_{Li} and μ_{Zr}) are

schematically shown by the green and violet spheres of Figure 6.

Figure 6 also includes a voltage scale, which relates directly to the Li chemical potential ($V = -\mu_{\text{Li}} \cdot e^-$). Negative μ_{Li} signify high voltages (vs Li/Li⁺) and vice versa.

Discussion

To gain realistic insights into the design of solid electrolytes for solid-state batteries, we have performed a thorough first-principles calculation analysis of the Li₇La₃Zr₂O₁₂ surfaces and its morphologies under various physical and chemical conditions.

Morphology and composition of Li₇La₃Zr₂O₁₂ particles – Figure 1b shows that lower surface energies are found for surfaces terminated by cations with lower oxidation states, following the trend Li⁺ < La³⁺ < Zr⁴⁺. This finding relates to electrostatic and geometric factors. By cleaving a cation-terminated surface, the large disruption of the ideal cation coordination environment results in a high-energy penalty, thus impacting significantly the relative stability of the surface.

Experimentally,⁵⁶ it is found that La³⁺ and Zr⁴⁺ ions prefer high oxygen coordination (≥ 6 in the cubic and tetragonal Li₇La₃Zr₂O₁₂ phases), whereas Li⁺ can adjust to both octahedral and tetrahedral environments.^{11,57} Li ions can tolerate reduced coordination environments leading to lower surface energies compared to Zr-terminated surfaces, which undergo a reduction in coordination from 6–8 to 4. La-terminated surfaces show low surface energies ($\sim 0.94 \text{ J m}^{-2}$) compared to the Zr-terminated surface, which are explained by the oxygen sub-layer stabilising the partially uncoordinated La atoms and lowering the surface energy (see Figure S3).

We have identified that surfaces with low Miller indices, e.g. (010) and (110) with Li-rich textures, dominate across a wide range of temperatures and oxygen environments. Li segregation at the surfaces of Li₇La₃Zr₂O₁₂ particles has been demonstrated by neutron depth profiling experiments.³⁹ O-terminated surfaces are also possible, as shown in Figure 6. This

may be significant in relation to the recent report of oxygen migration in $\text{Li}_7\text{La}_3\text{Zr}_2\text{O}_{12}$.⁵⁸

The predicted room temperature morphology of $\text{Li}_7\text{La}_3\text{Zr}_2\text{O}_{12}$ is in excellent agreement with a scanning electron microscopy study of a single crystal,⁴⁶ providing credibility to the computed morphologies of Figure 5. However, no specific surface facets were characterised, which we identified here.⁴⁶ We can complement the experimental observations by extending our model beyond the shape of the particles. This is completed by ascertaining the dominant surface facets and the most likely chemical compositions under both reducing and oxidising conditions.

On the basis of these findings we speculate that small cations, such as Al^{3+} and Ga^{3+} , doped at Li^+ sites may segregate at the surfaces of the particles. In agreement with our hypothesis, a number of experimental reports demonstrate that Al^{3+} segregates to the grain boundaries of doped $\text{Li}_7\text{La}_3\text{Zr}_2\text{O}_{12}$.^{55,59,60} We speculate that high-valent cations, such as Ta^{5+} and Bi^{5+} (introduced on the Zr lattice to increase the number of Li vacancies),¹¹ will constitute the core of the $\text{Li}_7\text{La}_3\text{Zr}_2\text{O}_{12}$ particles.

Densification and implications on ionic conductivity – Densification of ceramic oxides via high-temperature (and spark-plasma) sintering is routinely employed to improve the electrolyte ionic conductivity.^{11,45,55} Typically, the interpretation of impedance measurements requires the deconvolution of the total ionic conductivity into three main contributions, namely,^{61–63} intrinsic bulk, grain boundary and interfacial electrolyte/blocking electrode. While bulk Li-ion transport has been emphasised by both experiment and computation,^{7–9,11,31,32,47,51} grain boundary Li-ion conductivity is much less examined, despite being crucial.^{7–9,11}

The seminal paper on $\text{Li}_7\text{La}_3\text{Zr}_2\text{O}_{12}$ by Murugan *et al.*⁸ showed significant Li-ion resistance at the grain boundaries ($\sim 50\%$ of the total), thus suggesting the relevance of intergranular Li-ion transport.⁶⁴ Ceramic oxides processed at high temperatures containing “volatile” cations, such as Li, including $\text{Li}_7\text{La}_3\text{Zr}_2\text{O}_{12}$, will produce Li deficient bulk materi-

als,²⁷ and thus possible Li loss upon sintering treatments. For example, Antolini⁵⁴ showed that sintering of $\text{Li}_x\text{Ni}_{1-x}\text{O}$ ceramic electrodes can promote Li segregation at the particle exterior, thus altering the overall stoichiometry. Loss of Li_2O was observed in the synthesis of $\text{Li}_7\text{La}_3\text{Zr}_2\text{O}_{12}$,^{35,36,55,65} and additional Li_2O is routinely added during its preparation.

In agreement, our prediction in Figure 4 suggests that at high temperatures ($\geq 600^\circ\text{C}$ in the sintering regime) and reducing conditions, the particle surfaces will show pronounced segregation of Li. Assuming that the stable surfaces computed in this study are representative of the grain boundaries in $\text{Li}_7\text{La}_3\text{Zr}_2\text{O}_{12}$, we speculate that the accumulation of Li ions can impact the Li transport involving grain boundaries.⁶⁴

Engineering the particle morphology – On the basis of our predictions, we can propose practical strategies to engineer particle morphologies of $\text{Li}_7\text{La}_3\text{Zr}_2\text{O}_{12}$.

For example, Figure 6 demonstrates that adding extra Zr and/or Li metals during synthesis may promote Li segregation at the grain boundaries.³⁹ In addition, as indicated in Figure 4, routine high-temperature synthesis of $\text{Li}_7\text{La}_3\text{Zr}_2\text{O}_{12}$ promotes reducing conditions (i.e., oxygen-poor conditions) and Li terminated surfaces/particles. Hence low-temperature synthesis (and sintering) protocols should be sought.⁶⁶

From analysis of Figure 6, we speculate that O/La accumulation at the grains is also observed near the operating voltages of typical Li-ion cathode materials (e.g., $\text{LiCoO}_2 \sim 3.8\text{ V}$ vs. Li/Li^+ and $\text{LiFePO}_4 \sim 3.4\text{ V}$). In this context, Miara *et al.*⁶⁷ have shown that $\text{Li}_7\text{La}_3\text{Zr}_2\text{O}_{12}$ remains stable against LiCoO_2 , whereas the analogous interface with LiFePO_4 decomposes forming a protecting Li_3PO_4 interface. Nevertheless, a more recent experimental investigation by Goodenough *et al.*,⁶⁸ showed significant Al^{3+} and La^{3+} migration from Al-doped $\text{Li}_7\text{La}_3\text{Zr}_2\text{O}_{12}$ to LiCoO_2 , and negligible Zr diffusion into LiCoO_2 . In Figure 6, near 3 V we predict La segregation towards the particle surfaces corroborating these experimental findings.

The failure upon short-circuiting of polycrystalline $\text{Li}_7\text{La}_3\text{Zr}_2\text{O}_{12}$ in solid-state devices,

utilising a Li-metal anode, has been linked to dendrite propagation.²⁷ Near 0 V or at the potential of Li metal, we expect the $\text{Li}_7\text{La}_3\text{Zr}_2\text{O}_{12}$ particles to be lithium terminated. In agreement with our results, Li segregation close to a Li-metal anode interface in Al-doped $\text{Li}_7\text{La}_3\text{Zr}_2\text{O}_{12}$ has been recently observed by in situ transmission electron microscopy.³⁸ We speculate that the occurrence of Li at the particle surface and at grain boundaries, could indeed set the ideal chemical environment required for Li-dendrite growth and propagation between $\text{Li}_7\text{La}_3\text{Zr}_2\text{O}_{12}$ particles. In line with our results, Kerman *et al.*²⁷ proposed that once Li fills a crack in doped $\text{Li}_7\text{La}_3\text{Zr}_2\text{O}_{12}$, fresh electrodeposited Li extrudes to the existing grain boundaries.

Unsurprisingly, the process of dendrite propagation can originate from Li “stuffing” into grain boundaries.²⁷ Thus, the significant accumulation of Li at the surfaces of the $\text{Li}_7\text{La}_3\text{Zr}_2\text{O}_{12}$ particles may favour the initial stages of dendrite nucleation and growth along the existing grain boundaries. Further experimental studies are required to verify these hypotheses.

Conclusions

$\text{Li}_7\text{La}_3\text{Zr}_2\text{O}_{12}$ is an important solid electrolyte material, but its surfaces and particle morphologies under synthesis and sintering conditions are not fully characterised.

First, by studying the morphology and composition of $\text{Li}_7\text{La}_3\text{Zr}_2\text{O}_{12}$ particles from DFT-based calculations, we have demonstrated the spontaneous segregation of Li towards the particle exterior. Second, we map the compositional changes of the surfaces of $\text{Li}_7\text{La}_3\text{Zr}_2\text{O}_{12}$ as a function of temperature and of oxygen chemical pressure. Li segregation to surfaces is the dominant process over a range of temperatures, particularly during high-temperature synthesis and sintering. These findings are significant in relation to the initial stages of Li dendrite growth. Third, by studying the surface phase diagram of $\text{Li}_7\text{La}_3\text{Zr}_2\text{O}_{12}$, we find that Li segregation can be curbed by tuning the ceramic synthesis conditions. We show that

synthesis in reducing environments (O-poor, Li-rich and/or Zr-rich) may promote Li segregation to the particle surfaces. Finally, we find that particle compositions of $\text{Li}_7\text{La}_3\text{Zr}_2\text{O}_{12}$ are altered upon voltage sweeps, with Li segregation at the exterior occurring at the Li-metal anode voltage.

These findings will contribute towards developing strategies for the optimisation of the synthesis and operation of promising solid electrolytes for solid-state batteries.

Method

Surface energies and thermodynamic framework

The physical quantity defining stable surface compositions and geometries is the surface free energy γ (in J m^{-2}):

$$\gamma = \frac{1}{2A} \left[G_{\text{surface}} - G_{\text{bulk}} - \sum_i^{\text{species}} \Delta n_i \mu_i \right] \quad (1)$$

where A is the surface area (in m^{-2}) and G_{surface} and G_{bulk} are the surface free energies of periodic surfaces and the reference bulk material, respectively. G_{surface} and G_{bulk} are approximated by the respective computed internal energies E_{surface} and E_{bulk} , accessed by density functional theory (DFT) as described in the SI. In the case of non-stoichiometric surfaces, the final surface energy depends on the environment set by the chemical potential μ_i for species i and amounting to an off-stoichiometry of Δn_i . Note that Δn_i is negative (positive) if species i is removed (added) to the surface. The chemical potential references μ_i were derived from the computed phase diagram (Figure 1b) at 0 K.

Eq. 1 provides γ values at 0 K that are not representative for the operating conditions of solid electrolytes and the synthesis and sintering conditions. For non-stoichiometric surfaces, the approximation chosen to introduce the temperature dependence in the γ values is based on the fact that the surrounding O_2 atmosphere forms an ideal-gas-like reservoir, which is in equilibrium with $\text{Li}_7\text{La}_3\text{Zr}_2\text{O}_{12}$. The effect of temperature is introduced into the definition

of γ as follows:

$$\gamma(T) = \frac{1}{2A} \left[E_{\text{surface}} - E_{\text{bulk}} - \sum_i^{\text{species}-\{\text{O}\}} \Delta n_i \mu_i - \Delta n_{\text{O}} \mu_{\text{O}}(T) \right] \quad (2)$$

where μ_{O} is now a temperature dependent quantity and evaluated directly by combining DFT data with experimental values tabulated by NIST/JANAF as:⁶⁹

$$\mu_{\text{O}}(T) = \frac{1}{2} \mu_{\text{O}_2}(0 \text{ K, DFT}) + \frac{1}{2} \mu_{\text{O}_2}(0 \text{ K, Exp.}) + \frac{1}{2} \Delta G_{\text{O}_2}(\Delta T, \text{Exp.}) \quad (3)$$

where the $\mu_{\text{O}_2}(0 \text{ K, DFT})$ is the 0 K free energy of an isolated oxygen molecule evaluated with DFT, whereas $\mu_{\text{O}_2}(0 \text{ K, Exp.})$ is the 0 K experimental (tabulated) Gibbs energy for oxygen gas. $\Delta G_{\text{O}_2}(\Delta T, \text{Exp.})$ is the difference in the Gibbs energy defined at temperature, T , as $1/2[H(T, \text{O}_2) - H(0 \text{ K, O}_2)] - 1/2T[S(T, \text{O}_2)]$, respectively, as available in the NIST/JANAF tables.⁶⁹ We omitted the partial pressure dependence of the μ_{O_2} term (i.e., we used $p_{\text{O}_2} = 1 \text{ atm}$) as we expect this contribution to be small, as demonstrated previously.⁵³

Bulk surface models

Because of the large number of possible chemical terminations, as a result of the quaternary nature of $\text{Li}_7\text{La}_3\text{Zr}_2\text{O}_{12}$, the selection of surfaces investigated was only limited to low-index surfaces, such as (100), (001), (101), (111) and (201). We note that some of these surfaces are related by the intrinsic tetragonal symmetry. For example, (100) = (010), as verified by the surface energies in the Supplementary Information (see Table S2).

In line with Tasker’s classification of oxide surfaces,⁷⁰ only realistic type I surfaces were considered, which are characterised by zero charge and no electrical dipole moment. Nevertheless, these requirements are only satisfied by a limited number of stoichiometric Zr- or La-terminated surfaces with high surface energies.

Because our goal is to rationalise the chemical composition and morphology of the

$\text{Li}_7\text{La}_3\text{Zr}_2\text{O}_{12}$ particles, it is crucial to study the Li- and O-terminated surfaces. As a result, type I non-stoichiometric surfaces were generated by selectively removing layers of Zr and/or La and charge-compensated by O removal, as shown schematically in Figure 2. Upon cation removal, charge neutrality is maintained by introducing oxygen vacancies, resulting in the need to investigate a significant number of atomic orderings. We simplify this difficult task by computing with DFT only the 20 orderings with the lowest electrostatic energy, as obtained by minimising the Ewald energy of each surface using formal charges.⁷¹ This results in the assessment of 420 non-stoichiometric surfaces using DFT. While performing this operation, we enforce symmetry between the two faces of the surfaces. Using this strategy, we identified 21 non-stoichiometric orderings and 11 stoichiometric surfaces that are O-, Li-, La- and Zr-terminated, respectively, whose surface energies are discussed in Figure 3 and Table S2.

Acknowledgements

The authors gratefully acknowledge the EPSRC Programme Grant (EP/M009521/1) and the MCC/Archer consortium (EP/L000202/1). PC is grateful to the Ramsey Memorial Trust and University of Bath for the provision of his Ramsey Fellowship. PC is thankful to Dr. Benjamin Morgan at the University of Bath for fruitful discussions. PC deeply indebted to Dr. yet to be Theodosios Famprakis at the LRCS, Amiens, France. We acknowledge fruitful discussion with Prof. Peter Bruce, Stefanie Zekoll and Dr. Jitti Kasemchainan at the University of Oxford.

Supporting Information Available

The following files are available free of charge. The Supporting Information is available free of charge on the ACS Publications website at DOI:

- Details of first-principles calculations.
- Chemical potentials bounds.
- Surface energies.
- $\text{Li}_7\text{La}_3\text{Zr}_2\text{O}_{12}$ particle morphologies.
- $\text{Li}_7\text{La}_3\text{Zr}_2\text{O}_{12}$ surface reconstruction.

References

- (1) Armand, M.; Tarascon, J.-M. Building better batteries. *Nature* **2008**, *451*, 652–657.
- (2) Dunn, B.; Kamath, H.; Tarascon, J.-M. Electrical Energy Storage for the Grid: A Battery of Choices. *Science* **2011**, *334*, 928–935.
- (3) Islam, M. S.; Fisher, C. A. J. Lithium and sodium battery cathode materials: computational insights into voltage, diffusion and nanostructural properties. *Chem. Soc. Rev.* **2014**, *43*, 185–204.
- (4) Nykvist, B.; Nilsson, M. Rapidly falling costs of battery packs for electric vehicles. *Nat. Clim. Change* **2015**, *5*, 329–332.
- (5) Janek, J.; Zeier, W. G. A solid future for battery development. *Nat. Energy* **2016**, *1*, 16141.
- (6) Canepa, P.; Sai Gautam, G.; Hannah, D. C.; Malik, R.; Liu, M.; Gallagher, K. G.; Persson, K. A.; Ceder, G. Odyssey of Multivalent Cathode Materials: Open Questions and Future Challenges. *Chem. Rev.* **2017**, *117*, 4287–4341.
- (7) Thangadurai, V.; Kaack, H.; Weppner, W. J. F. Novel Fast Lithium Ion Conduction in Garnet-Type $\text{Li}_5\text{La}_3\text{M}_2\text{O}_{12}$ (M=Nb, Ta). *J. Am. Ceram. Soc.* **2003**, *40*, 437–440.

- (8) Murugan, R.; Thangadurai, V.; Weppner, W. Fast lithium ion conduction in garnet-type $\text{Li}_7\text{La}_3\text{Zr}_2\text{O}_{12}$. *Angew. Chem. Int. Ed.* **2007**, *46*, 7778–7781.
- (9) Knauth, P. Inorganic solid Li ion conductors: An overview. *Solid State Ion.* **2009**, *180*, 911–916.
- (10) Shinawi, H. E.; Janek, J. Stabilization of cubic lithium-stuffed garnets of the type " $\text{Li}_7\text{La}_3\text{Zr}_2\text{O}_{12}$ " by addition of gallium. *J. Power Sources* **2013**, *225*, 13–19.
- (11) Thangadurai, V.; Narayanan, S.; Pinzaru, D. Garnet-type solid-state fast Li ion conductors for Li batteries: critical review. *Chem. Soc. Rev.* **2014**, *43*, 4714–27.
- (12) Kamaya, N.; Homma, K.; Yamakawa, Y.; Hirayama, M.; Kanno, R.; Yonemura, M.; Kamiyama, T.; Kato, Y.; Hama, S.; Kawamoto, K.; Mitsui, A. A lithium superionic conductor. *Nat. Mater.* **2011**, *10*, 682–686.
- (13) Masquelier, C. Solid electrolytes: Lithium ions on the fast track. *Nat. Mater.* **2011**, *10*, 649–650.
- (14) Wang, Y.; Richards, W. D.; Ong, S. P.; Miara, L. J.; Kim, J. C.; Mo, Y.; Ceder, G. Design principles for solid-state lithium superionic conductors. *Nat. Mater.* **2015**, *14*, 1026–1031.
- (15) Bachman, J. C.; Muy, S.; Grimaud, A.; Chang, H.-h.; Pour, N.; Lux, S. F.; Paschos, O.; Maglia, F.; Lupart, S.; Lamp, P.; Giordano, L.; Shao-Horn, Y. Inorganic Solid-State Electrolytes for Lithium Batteries: Mechanisms and Properties Governing Ion Conduction. *Chem. Rev.* **2016**, *116*, 140–162.
- (16) Kato, Y.; Hori, S.; Saito, T.; Suzuki, K.; Hirayama, M.; Mitsui, A.; Yonemura, M.; Iba, H.; Kanno, R. High-power all-solid-state batteries using sulfide superionic conductors. *Nat. Energy* **2016**, *1*, 16030.

- (17) Deng, Y.; Eames, C.; Chotard, J.-N.; Lalère, F.; Seznec, V.; Emge, S.; Pecher, O.; Grey, C. P.; Masquelier, C.; Islam, M. S. Structural and mechanistic insights into fast lithium-ion conduction in $\text{Li}_4\text{SiO}_4\text{--Li}_3\text{PO}_4$ solid electrolytes. *J. Am. Chem. Soc.* **2015**, *137*, 9136–9145.
- (18) Mukhopadhyay, S.; Thompson, T.; Sakamoto, J.; Huq, A.; Wolfenstine, J.; Allen, J. L.; Bernstein, N.; Stewart, D. A.; Johannes, M. D. Structure and Stoichiometry in Super-valent Doped $\text{Li}_7\text{La}_3\text{Zr}_2\text{O}_{12}$. *Chem. Mater.* **2015**, *27*, 3658–3665.
- (19) Deng, Y.; Eames, C.; Fleutot, B.; David, R.; Chotard, J.-N.; Suard, E.; Masquelier, C.; Islam, M. S. Enhancing the Lithium Ion Conductivity in Lithium Superionic Conductor (LISICON) Solid Electrolytes through a Mixed Polyanion Effect. *ACS Appl. Mater. Interfaces* **2017**, *9*, 7050–7058.
- (20) Lotsch, B. V.; Maier, J. Relevance of solid electrolytes for lithium-based batteries: A realistic view. *J. Electroceram.* **2017**, *38*, 128–141.
- (21) Kim, J.-J.; Yoon, K.; Park, I.; Kang, K. Progress in the Development of Sodium-Ion Solid Electrolytes. *Small Methods* **2017**, *1*, 1700219.
- (22) Cheng, G.; Xu, Q.; Ding, F.; Sang, L.; Liu, X.; Cao, D. Electrochemical behavior of aluminum in Grignard reagents/THF electrolytic solutions for rechargeable magnesium batteries. *Electrochimica Acta* **2013**, *88*, 790–797.
- (23) Buschmann, H.; Dölle, J.; Berendts, S.; Kuhn, A.; Bottke, P.; Wilkening, M.; Heitjans, P.; Senyshyn, A.; Ehrenberg, H.; Lotnyk, A.; Duppel, V.; Kienle, L.; Janek, J. Structure and dynamics of the fast lithium ion conductor $\text{Li}_7\text{La}_3\text{Zr}_2\text{O}_{12}$. *Phys. Chem. Chem. Phys.* **2011**, *13*, 19378–19392.
- (24) Luntz, A. C.; Voss, J.; Reuter, K. Interfacial Challenges in Solid-State Li Ion Batteries. *J. Phys. Chem. Lett.* **2015**, *6*, 4599–4604.

- (25) Richards, W. D.; Miara, L. J.; Wang, Y.; Kim, J. C.; Ceder, G. Interface Stability in Solid-State Batteries. *Chem. Mater.* **2016**, *28*, 266–273.
- (26) Yu, C.; Ganapathy, S.; de Klerk, N. J. J.; Roslon, I.; van Eck, E. R. H.; Kentgens, A. P. M.; Wagemaker, M. Unravelling Li-Ion Transport from Picoseconds to Seconds: Bulk versus Interfaces in an Argyrodite $\text{Li}_6\text{PS}_5\text{ClLi}_2\text{S}$ All-Solid-State Li-Ion Battery. *J. Am. Chem. Soc.* **2016**, *138*, 11192–11201.
- (27) Kerman, K.; Luntz, A.; Viswanathan, V.; Chiang, Y.-M.; Chen, Z. Review Practical Challenges Hindering the Development of Solid State Li Ion Batteries. *J. Electrochem. Soc.* **2017**, *164*, A1731–A1744.
- (28) Yonemoto, F.; Nishimura, A.; Motoyama, M.; Tsuchimine, N.; Kobayashi, S.; Iriyama, Y. Temperature effects on cycling stability of Li plating/stripping on Ta-doped $\text{Li}_7\text{La}_3\text{Zr}_2\text{O}_{12}$. *J. Power Sources* **2017**, *343*, 207–215.
- (29) Porz, L.; Swamy, T.; Sheldon, B. W.; Rettenwander, D.; Frömling, T.; Thaman, H. L.; Berendts, S.; Uecker, R.; Carter, W. C.; Chiang, Y.-M. Mechanism of Lithium Metal Penetration through Inorganic Solid Electrolytes. *Adv. Energy Mater.* **2017**, 1701003.
- (30) Hanft, D.; Exner, J.; Moos, R. Thick-films of garnet-type lithium ion conductor prepared by the Aerosol Deposition Method: The role of morphology and annealing treatment on the ionic conductivity. *J. Power Sources* **2017**, *361*, 61–69.
- (31) Geiger, C. A.; Alekseev, E.; Lazic, B.; Fisch, M.; Armbruster, T.; Langner, R.; Fechtelkord, M.; Kim, N.; Pettke, T.; Weppner, W. Crystal Chemistry and Stability of $\text{Li}_7\text{La}_3\text{Zr}_2\text{O}_{12}$ Garnet: A Fast Lithium-Ion Conductor. *Inorg. Chem.* **2011**, *50*, 1089–1097.
- (32) Kuhn, A.; Narayanan, S.; Spencer, L.; Goward, G.; Thangadurai, V.; Wilkening, M. Li self-diffusion in garnet-type $\text{Li}_7\text{La}_3\text{Zr}_2\text{O}_{12}$ as probed directly by diffusion-induced ^7Li spin-lattice relaxation NMR spectroscopy. *Phys. Rev. B* **2011**, *83*, 094302.

- (33) Allen, J. L.; Wolfenstine, J.; Rangasamy, E.; Sakamoto, J. Effect of substitution (Ta, Al, Ga) on the conductivity of $\text{Li}_7\text{La}_3\text{Zr}_2\text{O}_{12}$. *J. Power Sources* **2012**, *206*, 315–319.
- (34) Adams, S.; Rao, R. P. Ion transport and phase transition in $\text{Li}_{7-x}\text{La}_3(\text{Zr}_{2-x}\text{M}_x)\text{O}_{12}$ ($\text{M} = \text{Ta}^{5+}, \text{Nb}^{5+}$, $x = 0, 0.25$). *J. Mater. Chem.* **2012**, *22*, 1426–1434.
- (35) Sharafi, A.; Haslam, C. G.; Kerns, R. D.; Wolfenstine, J.; Sakamoto, J. Controlling and correlating the effect of grain size with the mechanical and electrochemical properties of $\text{Li}_7\text{La}_3\text{Zr}_2\text{O}_{12}$ solid-state electrolyte. *J. Mater. Chem. A* **2017**, *5*, 21491–21504.
- (36) Yi, E.; Wang, W.; Kieffer, J.; Laine, R. M. Key parameters governing the densification of cubic- $\text{Li}_7\text{La}_3\text{Zr}_2\text{O}_{12}$ Li^+ conductors. *J. Power Sources* **2017**, *352*, 156–164.
- (37) Cheng, L.; Wu, C. H.; Jarry, A.; Chen, W.; Ye, Y.; Zhu, J.; Kostecki, R.; Persson, K.; Guo, J.; Salmeron, M.; Chen, G.; Doeff, M. Interrelationships among Grain Size, Surface Composition, Air Stability, and Interfacial Resistance of Al-Substituted $\text{Li}_7\text{La}_3\text{Zr}_2\text{O}_{12}$ Solid Electrolytes. *ACS Appl. Mater. Interfaces* **2015**, *7*, 17649–17655.
- (38) Ma, C.; Cheng, Y.; Yin, K.; Luo, J.; Sharafi, A.; Sakamoto, J.; Li, J.; More, K. L.; Dudney, N. J.; Chi, M. Interfacial Stability of Li Metal/Solid Electrolyte Elucidated via in Situ Electron Microscopy. *Nano Lett.* **2016**, *16*, 7030–7036.
- (39) Han, X.; Gong, Y.; Fu, K. K.; He, X.; Hitz, G. T.; Dai, J.; Pearse, A.; Liu, B.; Wang, H.; Rubloff, G.; Mo, Y.; Thangadurai, V.; Wachsman, E. D.; Hu, L. Negating interfacial impedance in garnet-based solid-state Li metal batteries. *Nat. Mater.* **2016**, *16*, 572–579.
- (40) Kim, Y.; Yoo, A.; Schmidt, R.; Sharafi, A.; Lee, H.; Wolfenstine, J.; Sakamoto, J. Electrochemical Stability of $\text{Li}_{6.5}\text{La}_3\text{Zr}_{1.5}\text{M}_{0.5}\text{O}_{12}$ ($\text{M} = \text{Nb}$ or Ta) against Metallic Lithium. *Front. Energy Res.* **2016**, *4*, 1–7.

- (41) Wang, C.; Gong, Y.; Dai, J.; Zhang, L.; Xie, H.; Pastel, G.; Liu, B.; Wachsman, E.; Wang, H.; Hu, L. In Situ Neutron Depth Profiling of Lithium Metal/Garnet Interfaces for Solid State Batteries. *J. Am. Chem. Soc.* **2017**, *139*, 14257–14264.
- (42) Kotobuki, M.; Munakata, H.; Kanamura, K.; Sato, Y.; Yoshida, T. Compatibility of $\text{Li}_7\text{La}_3\text{Zr}_2\text{O}_{12}$ Solid Electrolyte to All-Solid-State Battery Using Li Metal Anode. *J. Electrochem. Soc.* **2010**, *157*, A1076–A1079.
- (43) Sharafi, A.; Meyer, H. M.; Nanda, J.; Wolfenstine, J.; Sakamoto, J. Characterizing the Li- $\text{Li}_7\text{La}_3\text{Zr}_2\text{O}_{12}$ interface stability and kinetics as a function of temperature and current density. *J. Power Sources* **2016**, *302*, 135–139.
- (44) Wang, C.; Gong, Y.; Dai, J.; Zhang, L.; Xie, H.; Pastel, G.; Liu, B.; Wachsman, E.; Wang, H.; Hu, L. In Situ Neutron Depth Profiling of Lithium Metal-Garnet Interfaces for Solid State Batteries. *J. Am. Chem. Soc.* **2017**, *139*, 14257–14264.
- (45) Kingon, A. I.; Clark, J. B. Sintering of PZT Ceramics: I, Atmosphere Control. *J. Am. Ceram. Soc.* **1983**, *66*, 253–256.
- (46) Awaka, J.; Kijima, N.; Hayakawa, H.; Akimoto, J. Synthesis and structure analysis of tetragonal $\text{Li}_7\text{La}_3\text{Zr}_2\text{O}_{12}$ with the garnet-related type structure. *J. Solid State Chem.* **2009**, *182*, 2046–2052.
- (47) Miara, L. J.; Ong, S. P.; Mo, Y.; Richards, W. D.; Park, Y.; Lee, J.-M.; Lee, H. S.; Ceder, G. Effect of Rb and Ta Doping on the Ionic Conductivity and Stability of the Garnet $\text{Li}_{7+2xy}(\text{La}_{3x}\text{Rb}_x)(\text{Zr}_{2y}\text{Ta}_y)\text{O}_{12}$ ($0 \leq x \leq 0.375$, $0 \leq y \leq 1$) Superionic Conductor: A First Principles Investigation. *Chem. Mater.* **2013**, *25*, 3048–3055.
- (48) Thompson, T.; Yu, S.; Williams, L.; Schmidt, R. D.; Garcia-Mendez, R.; Wolfenstine, J.; Allen, J. L.; Kioupakis, E.; Siegel, D. J.; Sakamoto, J. Electrochemical Window of the Li-Ion Solid Electrolyte $\text{Li}_7\text{La}_3\text{Zr}_2\text{O}_{12}$. *ACS Energy Lett.* **2017**, *2*, 462–468.

- (49) Jain, A.; Ong, S. P.; Hautier, G.; Chen, W.; Richards, W. D.; Dacek, S.; Cholia, S.; Gunter, D.; Skinner, D.; Ceder, G.; Persson, K. A. Commentary: The Materials Project: A materials genome approach to accelerating materials innovation. *APL Mater.* **2013**, *1*, 011002.
- (50) Chen, M.-H.; Puchala, B.; der Ven, A. V. High-temperature stability of δ' -ZrO. *Calphad* **2015**, *51*, 292–298.
- (51) Burbano, M.; Carlier, D.; Boucher, F.; Morgan, B. J.; Salanne, M. Sparse Cyclic Excitations Explain the Low Ionic Conductivity of Stoichiometric $\text{Li}_7\text{La}_3\text{Zr}_2\text{O}_{12}$. *Phys. Rev. Lett.* **2016**, *116*.
- (52) Haase, F.; Sauer, J. The Surface Structure of Sulfated Zirconia: Periodic ab Initio Study of Sulfuric Acid Adsorbed on $\text{ZrO}_2(101)$ and $\text{ZrO}_2(001)$. *J. Am. Chem. Soc.* **1998**, *120*, 13503–13512.
- (53) Reuter, K.; Scheffler, M. Composition, structure, and stability of $\text{RuO}_2(110)$ as a function of oxygen pressure. *Phys. Rev. B* **2001**, *65*, 035406.
- (54) Antoini, E. Sintering of $\text{Li}_x\text{Ni}_{1-x}\text{O}$ solid solutions at 1200 °C. *J. Mater. Sci.* **1992**, *27*, 3335–3340.
- (55) Li, Y.; Cao, Y.; Guo, X. Influence of lithium oxide additives on densification and ionic conductivity of garnet-type $\text{Li}_{6.75}\text{La}_3\text{Zr}_{1.75}\text{Ta}_{0.25}\text{O}_{12}$ solid electrolytes. *Solid State Ionics* **2013**, *253*, 76–80.
- (56) Brown, I. D. What factors determine cation coordination numbers? *Acta Crystallogr. B* **1988**, *44*, 545–553.
- (57) Rong, Z.; Malik, R.; Canepa, P.; Sai Gautam, G.; Liu, M.; Jain, A.; Persson, K.; Ceder, G. Materials Design Rules for Multivalent Ion Mobility in Intercalation Structures. *Chem. Mater.* **2015**, *27*, 6016–6021.

- (58) Kubicek, M.; Wachter-Welzl, A.; Rettenwander, D.; Wagner, R.; Berendts, S.; Uecker, R.; Amthauer, G.; Hutter, H.; Fleig, J. Oxygen Vacancies in Fast Lithium-Ion Conducting Garnets. *Chem. Mater.* **2017**, *29*, 7189–7196.
- (59) Cheng, L.; Park, J. S.; Hou, H.; Zorba, V.; Chen, G.; Richardson, T.; Cabana, J.; Russo, R.; Doeff, M. Effect of microstructure and surface impurity segregation on the electrical and electrochemical properties of dense Al-substituted $\text{Li}_7\text{La}_3\text{Zr}_2\text{O}_{12}$. *J. Mater. Chem. A* **2014**, *2*, 172–181.
- (60) Ohta, S.; Kihira, Y.; Asaoka, T. Grain Boundary Analysis of the Garnet-Like Oxides $\text{Li}_{7+x-y}\text{La}_{3-x}\text{AXZr}_{2-y}\text{Nb}_y\text{O}_{12}$ (A = Sr or Ca). *Front. Energy Res.* **2016**, *4*.
- (61) Jamnik, J.; Maier, J. Treatment of the Impedance of Mixed Conductors Equivalent Circuit Model and Explicit Approximate Solutions. *J. Electrochem. Soc.* **1999**, *146*, 4183–4188.
- (62) Jamnik, J.; Maier, J. Generalised equivalent circuits for mass and charge transport: chemical capacitance and its implications. *Phys. Chem. Chem. Phys.* **2001**, *3*, 1668–1678.
- (63) Lai, W.; Haile, S. M. Impedance spectroscopy as a tool for chemical and electrochemical analysis of mixed conductors: A case study of ceria. *J. Am. Ceram. Soc.* **2005**, *88*, 2979–2997.
- (64) Dawson, J. A.; Canepa, P.; Famprakis, T.; Masquelier, C.; Islam, M. S. Atomic-Scale Influence of Grain Boundaries on Li-Ion Conduction in Solid Electrolytes for All-Solid-State Batteries. *J. Am. Chem. Soc.* **2017**, *140*, 362–368.
- (65) Kazyak, E.; Chen, K.-H.; Wood, K. N.; Davis, A. L.; Thompson, T.; Bielinski, A. R.; Sanchez, A. J.; Wang, X.; Wang, C.; Sakamoto, J.; Dasgupta, N. P. Atomic Layer Deposition of the Solid Electrolyte Garnet $\text{Li}_7\text{La}_3\text{Zr}_2\text{O}_{12}$. *Chem. Mater.* **2017**, *29*, 3785–3792.

- (66) Amores, M.; Ashton, T. E.; Baker, P. J.; Cussen, E. J.; Corr, S. A. Fast microwave-assisted synthesis of Li-stuffed garnets and insights into Li diffusion from muon spin spectroscopy. *J. Mater. Chem.A* **2016**, *4*, 1729–1736.
- (67) Miara, L. J.; Richards, W. D.; Wang, Y. E.; Ceder, G. First-principles studies on cation dopants and electrolyte—cathode interphases for lithium garnets. *Chem. Mater.* **2015**, *27*, 4040–4047.
- (68) Park, K.; Yu, B.-C.; Jung, J.-W.; Li, Y.; Zhou, W.; Gao, H.; Son, S.; Goodenough, J. B. Electrochemical Nature of the Cathode Interface for a Solid-State Lithium-Ion Battery: Interface between LiCoO_2 and Garnet- $\text{Li}_7\text{La}_3\text{Zr}_2\text{O}_{12}$. *Chem. Mater.* **2016**, *28*, 8051–8059.
- (69) Chase, M. W. *NIST-JANAF Thermochemical Tables 2 Volume-Set*; American Institute of Physics, 1998; p 1963.
- (70) Tasker, P. W. The stability of ionic crystal surfaces. *J. Phys. C: Solid State Phys.* **1979**, *12*, 4977–4984.
- (71) Ong, S. P.; Richards, W. D.; Jain, A.; Hautier, G.; Kocher, M.; Cholia, S.; Gunter, D.; Chevrier, V. L.; Persson, K. A.; Ceder, G. Python Materials Genomics (pymatgen): A robust, open-source python library for materials analysis. *Comput. Mater. Sci.* **2013**, *68*, 314–319.